DE GRUYTER Nanotechnology Reviews 2021; 10: 187–200

Research Article

Xiaoyu Zhao, Guannan Wang, Qiang Chen, Libin Duan, and Wenqiong Tu*

An effective thermal conductivity and thermomechanical homogenization scheme for a multiscale Nb_3Sn filaments

https://doi.org/10.1515/ntrev-2021-0015
received January 31, 2021; accepted March 22, 2021

Abstract: A comprehensive study of the multiscale homogenized thermal conductivities and thermomechanical properties is conducted towards the filament groups of European Advanced Superconductors (EAS) strand *via* the recently proposed Multiphysics Locally Exact Homogenization Theory (LEHT). The filament groups have a distinctive two-level hierarchical microstructure with a repeating pattern perpendicular to the axial direction of Nb_3Sn filament. The Nb_3Sn filaments are processed in a very high temperature between 600 and 700°C, while its operation temperature is extremely low, −269°C. Meanwhile, Nb_3Sn may experience high heat flux due to low resistivity of Nb_3Sn in the normal state. The intrinsic hierarchical microstructure of Nb_3Sn filament groups and Multiphysics loading conditions make LEHT an ideal candidate to conduct the homogenized thermal conductivities and thermomechanical analysis. First, a comparison with a finite element analysis is conducted to validate effectiveness of Multiphysics LEHT and good agreement is obtained for the homogenized thermal conductivities and mechanical and thermal expansion properties. Then, the Multiphysics LEHT is applied to systematically investigate the effects of volume fraction and temperature on homogenized thermal conductivities and thermomechanical properties of Nb_3Sn filaments at the microscale and mesoscale. Those homogenized properties provide a full picture for researchers or engineers to understand the Nb_3Sn homogenized properties and will further facilitate the material design and application.

Keywords: Nb_3Sn filaments, thermal conductivity, thermomechanical analysis, hierarchical microstructures, multiphysics locally exact homogenization theory, multiscale homogenization

1 Introduction

A variety of high-performance superconducting wires [1–4] has been actively pursued and developed to meet the requirements of different engineering applications. Nb_3Sn superconducting wire strand has superior critical temperature and field, which has been widely used for next-generation magnets for high-energy physics and fusion, including the KSTAR tokamak in South Korea [5], ITER CS model in Japan [6], a high-field Very Large Hadron Collider (VLHC) [7], ITER [1,2,8,9], as well as many other applications above 13 T [10–12]. Nb_3Sn is brittle and strain-sensitive and is not suitable for extrusion [2,13,14]. The material is manufactured by first inserting uncompounded precursors of Nb_3Sn into an ingot of bronze, then the ingot is drawn into a wire and finally the heat treatment is conducted to form Nb_3Sn filaments. The typical heat treatment requires hundreds of hours between 600 and 700°C in a vacuum or inert gas to prevent bronze from oxidation [13]. The superconductor strand serves as the basic building block for the superconducting cables, such as cable-in-conduit conductors (CICC), Rutherford cables [7], which are designed and manufactured based on the specific commercial or scientific applications. For instance, CICC is utilized for ITER and over thousand strands are twisted together following a multistage packaging process and then inserted into a metal jacket which

---

*** Corresponding author: Wenqiong Tu,** Department of Vehicle Engineering, School of Automotive and Traffic Engineering, Jiangsu University, Zhenjiang 212013, China, e-mail: wtu@ujs.edu.cn
Xiaoyu Zhao: Department of Automotive Engineering, School of Mechanical and Automotive Engineering, Shanghai University of Engineering Science, Shanghai 201620, China
Guannan Wang: Center for Balanced Architecture, Zhejiang University, Hangzhou 310007, China; Department of Civil Engineering, Zhejiang University, Hangzhou 310058, China
Qiang Chen: Arts et Métiers Institute of Technology, CNRS, Universitéde Lorraine, LEM3-UMR7239, Metz F-57000, France
Libin Duan: Department of Vehicle Engineering, School of Automotive and Traffic Engineering, Jiangsu University, Zhenjiang 212013, China

sustains the magnetic load and contains the liquid helium (4.2 K) during the operation stage [15].

Nb_3Sn strand contains many Nb_3Sn filaments, which possess complicated hierarchical microstructures [15–18]. Nb_3Sn filaments are processed in a high temperature (600–700°C) and operate under an extremely low temperature (−269°C). An effective Multiphysics micromechanics model to predict the thermal conductivities and thermomechanical properties of the Nb_3Sn strands would accelerate the material development, reduce the cost of material characterization, and further facilitate the cable analysis and design [19–22]. In general, the micromechanics methods can be categorized into two categories [19] (Pindera *et al.* 2009). One is the microstructural detail-free estimates which do not consider the actual geometry of the material microstructures. In contrast, another one considers the real microstructures of the materials. The classic approaches fall into microstructural detail-free category, such as Reuss and Voigt estimates, self-consistent scheme, general self-consistent scheme, Mori-Tanaka scheme, Composite Spherical/Cylinder model (CCA and CSA), and Halpin-Tsai theory [19,23–25]. For instance, general self-consistent scheme [15] and Mori-Tanaka scheme [26] are utilized to estimate the effective mechanical and thermal expansion properties for the Furukawa strand. In the category of considering material's real microstructures, Finite Element Approach (FEA) has become the main approach to calculate the homogenized properties of Nb_3Sn filament groups *via* a 3D Representative Volume Element (RVE) [13,17,27–30] due to its ability to consider complex microstructures in great detail and the popularity of general commercial FEA software represented by ABAQUS and ANSYS.

In finite element framework, the geometric microstructures are divided into subregions in which the local displacement fields are approximated by shape functions. A large system of algebraic equations for the unknown coefficients in the local approximations is constructed by satisfying the governing field equations using variational approach. In the field of multiscale homogenization analysis, the computational cost could increase dramatically because each material point at the upper scale is represented by a microstructure in the lower scale. The Multiphysics Locally Exact Homogenization Theory (MLEHT), an analytical approach, possesses great potential to determine the homogenized thermal conductivities and thermomechanical properties and recover the local fields in an efficient and accurate way. LEHT is initially developed by Pindera and coworkers for the hygro-thermomechanical responses of unidirectional composites [16,31,32] and has been extensively validated against FEA [31,32] and Finite Volume approach [16,32]. LEHT is a natural fit for the homogenization of Nb_3Sn filament groups. First, LEHT is a Multiphysics homogenization approach which can cope with the Multiphysics phenomenon for Nb_3Sn filaments, including Heat transfer and thermomechanical loading. Secondly, the Nb_3Sn filaments usually possess a distinctive hierarchical microstructure and multiscale homogenization is required to predict the effective properties and LEHT has been proven itself as an idea candidate for the multiscale applications due to its distinctive features of user-friendliness, accuracy, and efficiency [32]. First, LEHT is an analytical approach without the need of time-consuming preprocessing and post-processing of widely utilized commercial software. The method utilizes Fourier series expansions to represent the displacement fields. Secondly, the equilibrium equations and continuity conditions are satisfied in an exact way based on the method's analytical nature, so the method's accuracy is guaranteed from the fundamental level without the worry of mesh convergence. Thirdly, a balanced variational principle is applied for the periodic boundary condition of repeating unit cells to ensure rapid convergence of the Fourier series coefficients with a relatively small number of harmonic terms [31]. A full set of homogenized thermal conductivities and thermomechanical properties can be generated in less than 10 s on a personal computer.

The rest of the manuscript is organized as follows: Section 2 establishes a hierarchical model for the European Advanced Superconductors (EAS) Nb_3Sn filament groups utilized for the ITER D-shaped magnet. Section 3 summarizes the key steps of Multiphysics LEHT, including Distinguishment of the Homogenized and Localized Responses, Derivation of Internal Expressions, Imposition of Continuity Conditions, Implementation of Periodic Boundary Conditions, Establishment of Homogenizations, and Encapsulation of Multiphysics LEHT. Section 4 validates the LEHT's effectiveness in predicating the homogenized thermal conductivities and thermomechanical properties against FEA prediction. Following the method validation, section 5 conducts a systematic investigation towards the effects of volume fraction and temperature on the two-scale homogenized thermal conductivities and thermomechanical properties. Section 5 concludes this presentation.

2 Model establishment

The hierarchical structure of an EAS strand, illustrated in Figure 1, can be analyzed from a multiscale perspective. First of all, a global cross section of an EAS strand is

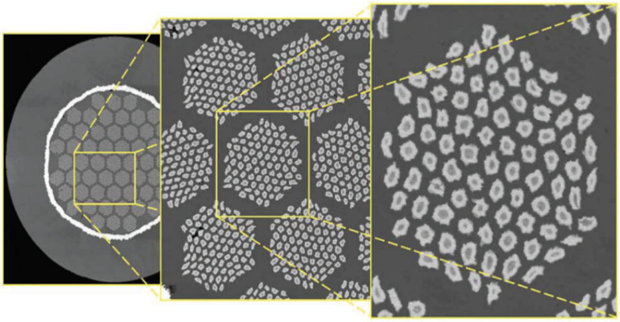

Figure 1: The hierarchical structure of an EAS strand: the macroscale structure of the global strand (Left), the mesoscale structure of the filament groups (Center), and the microscale structure of the filament (Right). (Reprinted from ref. [13], with copyright permission from Elsevier).

illustrated in Figure 1 (left) at the macroscale, containing the outer copper matrix, tantalum thick barrier, and around 55 groups of filaments, which are periodically arrayed in a bronze matrix. To facilitate the macroscale analysis, the thermal conductivities and thermoelastic properties of those mesoscale groups of filaments (Figure 1 center) can be further characterized through the microscale unit cells that contain about 85 polygonal Nb_3Sn filaments embedded in the bronze matrix, see Figure 1 (right). The single filament diameter is 2–5 µm, the diameter of a group of filaments is about 55–60 µm [13], and tantalum barrier diameter is 0.507 mm [15]. It is seen that the Nb_3Sn filaments or filament groups are all periodically laid out in a hexagonal fashion, producing the isotropic in-plane properties, just shown as Figures 2 and 3 magnify the mesoscale structure of filament groups (Figure 1 center) and microscale structure of a group of filaments (Figure 1 right) that are mapped in periodically hexagonal fashion (that are characterized by the yellow highlight). A multiscale LEHT framework is employed to generate the homogenized thermal conductivities and thermomechanical properties of unit cells of different scales.

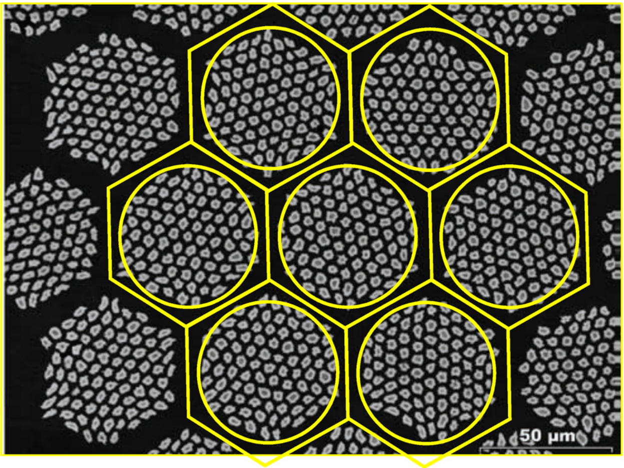

Figure 2: Mesoscale structure of multiple filament groups and corresponding hexagonal unit cell representation. (Reprinted from ref. [13], with copyright permission from Elsevier).

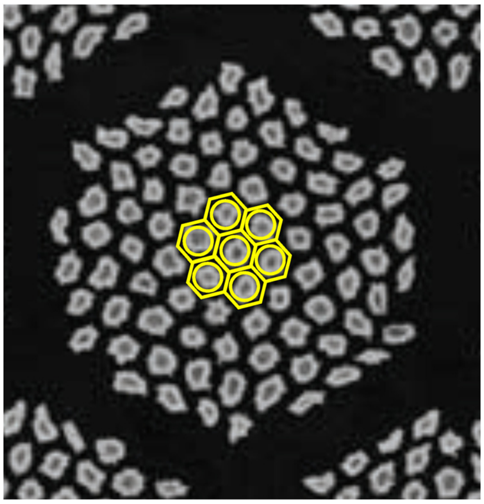

Figure 3: Microscale structure of a filament group and corresponding hexagonal unit cell representation. (Reprinted from ref. [13] with copyright permission from Elsevier).

3 Overview of multiscale LEHT

Relative to other micromechanics models, the theoretical development of the LEHT is mainly based on the Trefftz concept, where the internal expressions of thermal conductivities or mechanical fields of the composites' constituents are first obtained through solving the partial differential equations, whose solutions are represented through series expansions. The internal expressions with unknown coefficients are solved through imposing the continuity conditions at the fiber–matrix interface, as well as the weak-form periodic boundary conditions. The effective coefficients of a composite are finally derived through the homogenization theory. The macroscale properties of an EAS strand with two-level hierarchical microstructures can be obtained through a two-level multiscale homogenization process. First, the effective properties of a group of Nb_3Sn filaments can be obtained through a homogenization process at microscale. Then the calculated homogenized properties are fed into the analysis of mesoscale unit cell, from which the effective properties of the EAS strand at macroscale are predicted. In contrast, the localization process passes down loads from macroscale to microscale. The local stress and strain fields of a mesoscale unit cell are predicted once the macroscale strain/stress is specified. Then the local stress/strain fields of a microscale unit cell are determined by applying the corresponding mesoscale stress/strain. The date flow of multiscale homogenization and location of hierarchical microstructures of Nb_3Sn strand are shown in Figure 4.

The general steps of LEHT are overviewed in this section for the readers' interests:

3.1 Step 1: Distinguishment of the homogenized and localized responses

In this presentation, we establish a two-scale homogenization framework with microstructures. Thus, herein we define each upper scale as the homogenized scale, while its lower scale as the localized microstructure. The homogenized properties of the upper scale are obtained through homogenization of the lower-scale microstructure, while the homogenized response of upper scale is transmitted to stimulate the lower-scale reaction. For instance, the governing equations (1) and (2) for temperature $T(x, y)$ and the displacement fields $u_i(x, y)$ can be decomposed into the homogenized and fluctuating parts:

Thermal conductivities [33]:

$$T(x, y) = \bar{T}(x) + T'(y) \tag{1}$$

Thermomechanical behavior [16,32]:

$$u_i(x, y) = \bar{u}_i(x) + u'_i(y), \quad (i = 1, 2, 3) \tag{2}$$

where $x = (x_1, x_2, x_3)$ and $y = (y_1, y_2, y_3)$ are the upper-scale homogenized and lower-scale localized coordinates, respectively. $i = 1$ is longitudinal direction, while $i = 2,3$ is transverse cross section. The average and fluctuating parts denote the homogenized and localized responses, respectively.

3.2 Step 2: Derivation of internal expressions

To recover the localized response within lower-scale microstructure, the solutions of the governing partial differential equations for fluctuating fields presented in the Appendix are obtained by adopting the series functions [16,32,33]:

Thermal conductivities:

$$T'^{(i)} = \sum_{n=0}^{\infty}[(r^n I^i_{n1} + r^{-n} I^i_{n3})\cos n\theta + (r^n I^i_{n2} + r^{-n} I^i_{n4})\sin n\theta] \tag{3}$$

Thermomechanical behavior:

$$u'^{(i)}_z = \sum_{n=1}^{\infty}[(r^n H^i_{n1} + r^{-n} H^i_{n3})\cos n\theta + (r^n H^i_{n2} + r^{-n} H^i_{n4})\sin n\theta] \tag{4a}$$

$$u'^{(i)}_r = F^i_{01} r + F^i_{02} r^{-1} + \sum_{n=2}^{\infty}\sum_{j=1}^{4} r^{p_{nj}}[F^i_{nj}\cos n\theta + G^i_{nj}\sin n\theta] \tag{4b}$$

$$u'^{(i)}_\theta = \sum_{n=2}^{\infty}\sum_{j=1}^{4} \beta_{nj} r^{p_{nj}}[F^i_{nj}\sin n\theta - G^i_{nj}\cos n\theta] \tag{4c}$$

where the superscript "i" can be the "f" (fiber phase) or "m" (matrix phase). r is the parameter of fiber radius and can be utilized as a dimensional parameter, β_{nj} and p_{nj} are the eigenvalues and eigenvectors that are obtained in solving the differential governing equations listed in the

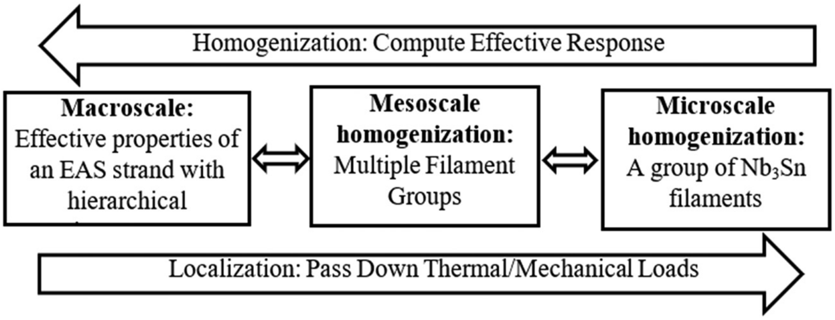

Figure 4: Date flow of multiscale homogenization and location of hierarchical microstructures of Nb_3Sn strand.

Appendix. Note that several unknown coefficients, I_{nj}, H_{nj}, F_{nj}, G_{nj} in the equations (3) and (4) are introduced and need to be obtained through the continuity and boundary conditions in the following steps. What's more, the expressions of heat fluxes (*e.g.*, q_r, q_θ) and stress–strain (*e.g.*, σ_{zr}, σ_{rr}, $\sigma_{r\theta}$) fields are also readily derived.

3.3 Step 3: Imposition of continuity conditions

The aforementioned solutions are explicitly expressed in the cylindrical coordinates for the easiness of imposing continuities. For a perfectly bonded interface, the continuities are established at the fiber–matrix interface:

Thermal conductivities:

$$T'^{(f)} = T'^{(m)}|_{r=a} \tag{5a}$$

$$q_r^{(f)} = q_r^{(m)}|_{r=a} \tag{5b}$$

Thermomechanical behavior:

$$u'^{(f)}_z = u'^{(m)}_z|_{r=a}, \quad \sigma^{(f)}_{zr} = \sigma^{(m)}_{zr}|_{r=a} \tag{6a}$$

$$u'^{(f)}_r = u'^{(m)}_r|_{r=a}, \quad \sigma^{(f)}_{rr} = \sigma^{(m)}_{rr}|_{r=a} \tag{6b}$$

$$u'^{(f)}_\theta = u'^{(m)}_\theta|_{r=a}, \quad \sigma^{(f)}_{r\theta} = \sigma^{(m)}_{r\theta}|_{r=a} \tag{6c}$$

from which the unknown fiber coefficients are expressed in terms of matrix coefficients, where a denotes the radius of inhomogeneity.

3.4 Step 4: Implementation of periodic boundary conditions

For unit cells that are periodically arranged within the lower levels, the periodic boundary conditions need to be imposed. In this work, weak-form boundary conditions are employed to guarantee the numerical stability:

Thermal conductivities [33]:

$$\int_{S_Q} \delta T(Q - Q^0)\mathrm{d}S + \int_{S_T} \delta Q(T - T^0)\mathrm{d}S = 0 \tag{7}$$

where $Q(S_j) = \int_{S_j} q_i n_i \mathrm{d}S$. $Q = Q^0$ and $T = T^0$ are the periodicities of heat flux and temperature components. n_i is the unit normal of surface $S_j\,(j = 1, 2, \ldots, 6)$ of hexagonal unit cells.

Thermomechanical behavior [34]:

$$\int_{S_t} \delta u_i\,(t_i - t_i^0)\mathrm{d}S + \int_{S_u} \delta t_i\,(u_i - u_i^0)\mathrm{d}S = 0 \tag{8}$$

where $t_i(S_j) = \int_{S_j} \sigma_{ik} n_k \mathrm{d}S$. $u_i = u_i^0$ and $t_i = t_i^0$ are the periodicities of displacement and stress components.

From which all the remaining unknowns can be obtained. Then the internal thermal and mechanical distributions can be fully recovered.

3.5 Step 5: Establishment of homogenizations

The effective thermal and elastic coefficients at higher levels can be generated through generalized homogenized equations:

Fourier's law of heat conduction:

$$\bar{q}_i = -K^\star_{ij}\bar{H}_j \tag{9}$$

Homogenized constitutive relation:

$$\bar{\sigma}_{ij} = C^\star_{ijkl}\{\bar{\varepsilon}_{kl} - \alpha^\star_{ij}\Delta T\} \tag{10}$$

where, $\bar{q}_i$ and $\bar{H}_j$ are the effective heat flux component and temperature gradient, respectively, while $\bar{\sigma}_{ij}$ and $\bar{\varepsilon}_{kl}$ are the stress and strain components, respectively. ΔT is the change of temperature, the K^*_{ij}, C^*_{ijkl}, and α^*_{ij} are the effective thermal conductivities, elastic, and thermal expansion matrices, respectively, from which the thermal conductive and thermoelastic coefficients in all directions can be readily obtained.

3.6 Step 6: Encapsulation of Multiphysics LEHT

The advantage of adopting the Trefftz concept in the LEHT is that the mesh discretization and pre- and post-processing are avoided in the in-house MATLAB programs. Based on this point, we encapsulated the program into "black-boxes" with only input/output (I/O) connections [32]. Users only need to input the geometric and material properties of the composite materials and the programs will automatically generate the effective coefficients and localized responses within a few seconds. Based on the theoretical derivations, we developed our own in-house programs to conduct numerical validations and parametric investigations.

4 Validation

To validate Multiphysics LEHT's effectiveness to predict the homogenized thermal conductivities, mechanical and thermal expansion coefficient generated *via* Multiphysics LEHT has been compared against the results generated

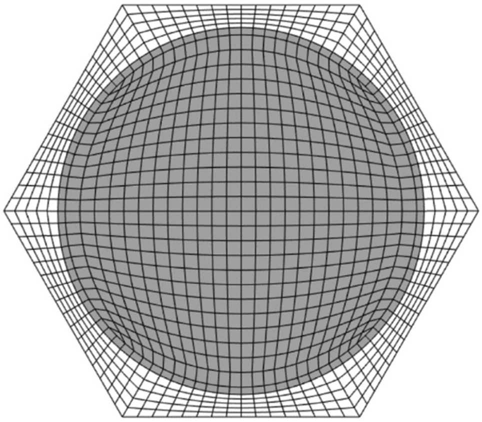

Figure 5: Mesh of a hexagonal unit cell with v_f = 0.72.

by ABAQUS-based FEA [13] and an in-house FEA calculation [35–37]. Figure 5 shows the mesh utilized in our in-house FEA analysis. A fully anisotropic two-dimensional Q8-type Multiphysics quadratic element has been constructed under the generalized plane strain constraint and the element number is 1152.

4.1 Thermal conductivity analysis

Figure 6 illustrates the comparison of homogenized axial thermal conductivity, $K_{11}^{\star}$, and transverse thermal conductivities, $K_{22}^{\star}$, $K_{33}^{\star}$, between LEHT and Boso's FEA predictions [13] for the hexagonal unit cell at microscale, in which Nb_3Sn is surrounded by the bronze matrix, as shown in Figure 3. Nb_3Sn's thermal conductivity is insensitive to the temperature variation and its value is exceedingly small. The Poisson's ration of Nb_3Sn is 0.3 [27]. In contrast, bronze possesses an interesting characteristic regarding its thermal conductivity towards the temperature variation. In general, the thermal conductivity's variation caused by the temperature change could be divided into three stages. Initially, the thermal conductivity increases dramatically from 0 K and reaches a peak value, 2,400 W/(m K) at 33.3 K, and then decreases sharply to 1,000 W/(m K) at 55 K. In the second stage between 55 and 200 K, bronze's thermal conductivity decreases gradually and reach a stable value of 386 W/(m K) at 200 K. During the rest of temperature variation, the thermal conductivity almost maintains a constant value, 386 W/(m K). And the Poisson's ratio of Bronze is 0.34 [27].

The volume fraction of Nb_3Sn for unit cell at microscale is 0.24. It should be noticed that Boso *et al.* [13] utilized two different volume fractions at microscale for the calculation of axial thermal conductivity, $K_{11}^{\star}$, and the transverse thermal conductivities, $K_{22}^{\star}$, $K_{33}^{\star}$: volume fraction 0.7 is utilized for $K_{11}^{\star}$'s calculation and 0.24 is utilized for $K_{22}^{\star}$'s and $K_{33}^{\star}$'s estimation. To maintain consistency, the volume fraction 0.24 is utilized to calculate both axial and transverse thermal conductivity calculations. The homogenized axial thermal conductivity, $K_{11}^{\star}$, is compared with Rule of Mixture's (RoM) estimation and the homogenized transverse thermal conductivities, $K_{22}^{\star}$ and $K_{33}^{\star}$ are compared with Boso *et al.* prediction [13]. Meanwhile, in Boso's estimation [13], a quasi-hexagonal unit cell is utilized for the analysis, but $K_{22}^{\star}$'s and $K_{33}^{\star}$'s predictions are almost identical. Out of simplicity, a hexagonal unit cell is utilized in our analysis and the homogenized transverse thermal conductivity $K_{22}^{\star}$ is equal to $K_{33}^{\star}$. Figure 6 shows excellent agreement between LEHT's prediction and Boso *et al.* FEA [13] estimation for the transverse thermal conductivities, $K_{22}^{\star}$ and $K_{33}^{\star}$, and between LEHT's prediction and Rule of Mixture's (RoM) estimation for the axial thermal conductivity, $K_{11}^{\star}$.

After obtaining the homogenized thermal conductivities for the RUC representing a filament group at

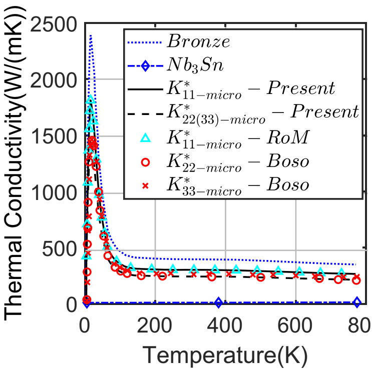

Figure 6: Comparison of homogenized thermal conductivity generated by LEHT and FEA [13] with v_f = 0.24 for Nb_3Sn filaments at microscale.

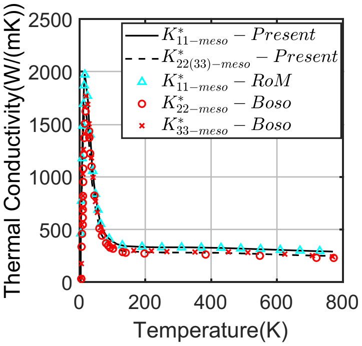

Figure 7: Comparison of homogenized thermal conductivity generated by LEHT and Boso *et al.* [13] with v_f = 0.72 for multiple filament groups at mesoscale.

microscale, the homogenization of all filament groups at mesoscale could be conducted for a hexagonal unit cell in which a homogenized filament group is embedded in the bronze matrix, as illustrated in Figure 2. Figure 7 illustrates the comparison of transverse thermal conductivities, $K_{22}^{\star}$ and $K_{33}^{\star}$, generated LEHT and Boso *et al.* FEA predictions [13] and the comparison of homogenized axial thermal conductivity, $K_{11}^{\star}$, calculated by LEHT and the Rule of Mixture (RoM) with volume fraction of 0.72 at mesoscale. Good agreement for both axial and transverse conductivity coefficients is obtained. Therefore, the accuracy of the LEHT in predicting the homogenized thermal conductivity is validated for both a filament group at microscale and multiple filament groups at mesoscale. Also, its worth to mention there is no laborious work involved in LEHT's prediction, such as mesh discretization, periodic boundary imposition, and post-processing for homogenization properties as in Boso's calculation in ABAQUS with 3D FEA model and only unit cell geometric information and constituents' properties are required. Meanwhile, LEHT's calculation is highly efficient due to its trait of an analytical solution and only 0.7 s is required to generate a full set of homogenized thermal conductivities on a PC with Windows 10 64-bit operation system, Intel 2.9 GHz i7-10700 CPU, and 16 GB RAM.

4.2 Thermomechanical analysis

Figure 8 illustrates the comparison of homogenized mechanical properties and thermal expansion coefficients between LEHT's and Boso *et al.* FEA predictions for unit cell with volume fraction of 0.42 for Nb_3Sn filament at microscale. Nb_3Sn's main diagonal elasticity term is not sensitive to temperature change, but the elasticity term of matrix material, Bronze, decreases significantly as the increase of temperate till 500 K and then maintain a constant value of 80 GPa. Regarding the thermal expansion coefficients, both Nb_3Sn and filament phases increase linearly as the temperature increases. Figure 8 (Left) shows good agreement between LETH's and Boso *et al.* [13] prediction for the homogenized diagonal elasticity terms, $D_{11}^{\star}$, $D_{22}^{\star}$, $D_{33}^{\star}$. Figure 8 (Right) shows good agreement for the homogenized axial thermal expansion coefficient, $\alpha_{11}^{\star}$, and the transverse homogenized thermal expansion coefficients, $\alpha_{22}^{\star}$, $\alpha_{33}^{\star}$, generated by LEHT and Boso *et al.* [13].

After obtaining the Nb_3Sn homogenized mechanical properties and thermal expansion coefficients for the RUC representing a filament group at microscale, the homogenization of multiple filament groups at mesoscale could be conducted for the hexagonal RUC in which a homogenized filament group is embedded in the bronze matrix. It should be noticed that in Boso's FEA estimation, volume fraction 0.72 is utilized to generate all homogenized mechanical properties, but volume fraction 0.90 is utilized to generate all the homogenized thermal expansion, $\alpha_{22}^{\star}$, $\alpha_{33}^{\star}$, except $\alpha_{11}^{\star}$, Figure 9 (Right). To maintain consistency, volume fraction 0.72 is utilized to calculate all homogenized thermomechanical properties in LEHT. As shown in Figure 9 (Left), good agreement is obtained for the homogenized mechanical properties at mesoscale. To further validate LEHT's thermomechanical homogenization capability, an in-house FEA program [35–37] is utilized to calculate the homogenized main diagonal elasticity terms and the thermal expansion coefficients, as shown in Figure 10, and excellent agreement is achieved. Therefore, the effectiveness of the LEHT in predicting the

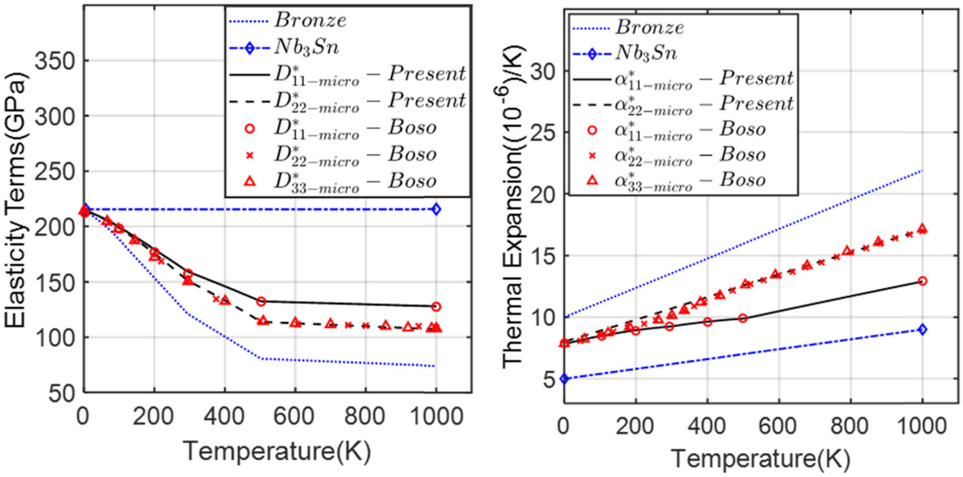

Figure 8: Comparison of homogenized main diagonal elasticity terms (Left) and thermal expansion coefficients (Right) generated by LEHT and Boso *et al.* [13] with $v_f = 0.42$ for Nb_3Sn filaments at microscale.

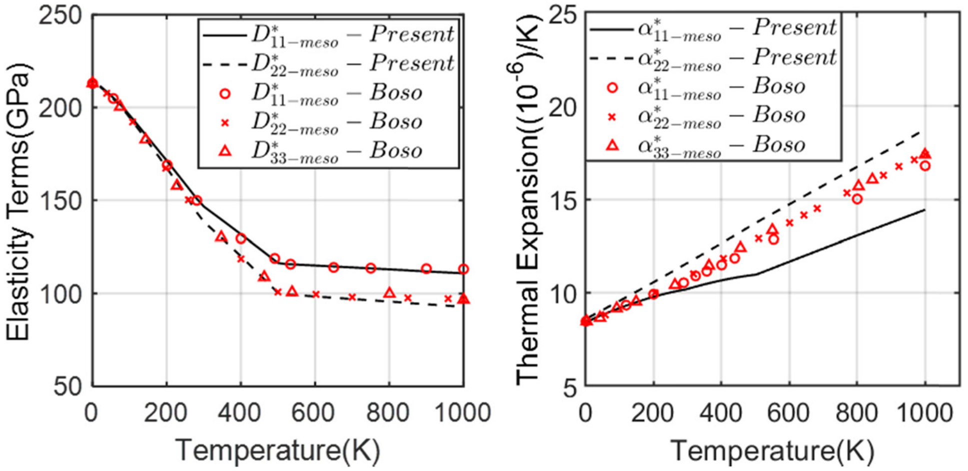

Figure 9: Comparison of homogenized main diagonal elasticity terms (Left) and thermal expansion coefficients (Right) generated by LEHT and Boso *et al.* [13] with $v_f = 0.72$ at mesoscale.

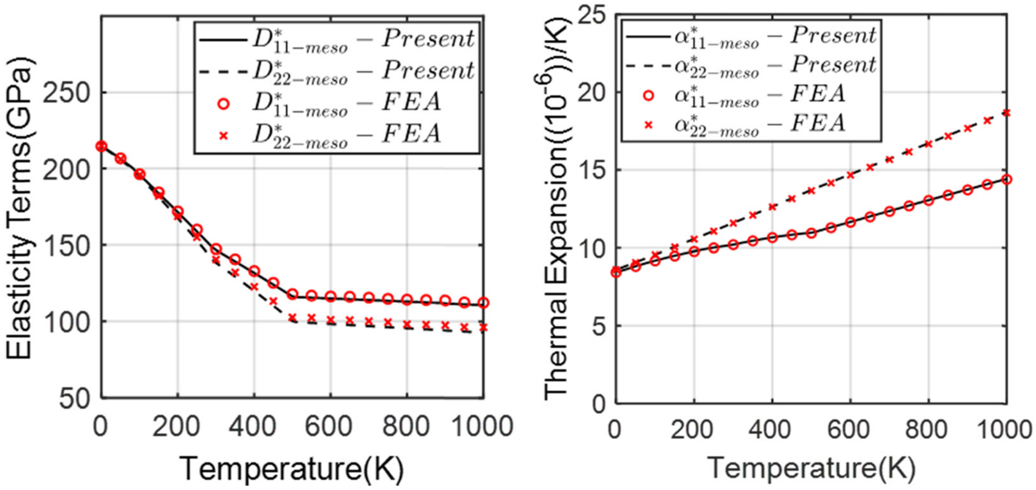

Figure 10: Comparison of homogenized main diagonal elasticity terms (Left) and thermal expansion coefficients (Right) generated by LEHT and in-house FEA with $v_f = 0.72$ at mesoscale.

homogenized mechanical properties and thermal expansion coefficients at both microscale and mesoscale levels is validated. Meanwhile, as the homogenization of thermal conductivity, the thermomechanical homogenization is very efficient and only 17 s is utilized to calculate the homogenized thermomechanical properties on a PC with Windows 10 64-bit operation system, Intel 2.9 GHz i7-10700 CPU, and 16 GB RAM. The efficiency facilitates the proposed technique in the material's design and practice, especially when combined with the optimization technique. It should also be pointed out that when validating against the FE-based ABAQUS simulations, we employ a different strategy. For instance, here we didn't employ the mesh discretization, but directly obtain the analytical internal solutions. We also utilize the weak-form variational principle to enforce the boundary periodicities, while ABAQUS directly impose periodic boundary conditions in a node-to-node fashion.

5 Results

5.1 Effects of volume fraction and temperature on homogenized thermal conductivities

Figure 11 illustrates the effect of volume fraction of a Nb_3Sn filament at microscale on the homogenized axial

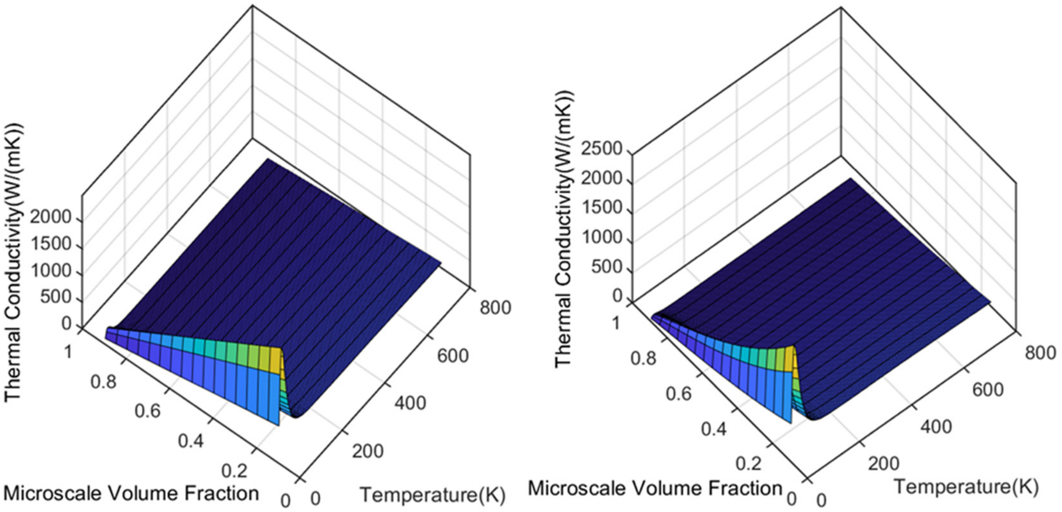

Figure 11: Effects of volume fraction of Nb_3Sn filament at microscale and temperature on homogenized thermal conductivity, (Left) $K_{11}^{\star}$, (Right) $K_{22}^{\star}(K_{33}^{\star})$.

thermal conductivity $K_{11}^{\star}$ and transverse thermal conductivities $K_{22}^{\star}$ and $K_{33}^{\star}$ between 5 and 800 K. At a given temperature, the homogenized axial thermal conductivity, $K_{11}^{\star}$, decreases linearly as the increase of volume fraction since its value follows the rule of mixture. The lower bound of $K_{11}^{\star}$ converges to the thermal conductivity of Nb_3Sn at volume fraction 1 and the upper bound converges to the thermal conductivity of bronze at volume fraction 0. Similar with the axial thermal conductivity, the transverse thermal conductivities $K_{22}^{\star}(K_{33}^{\star})$ also decreases as the increase of volume fraction and the lower bound of $K_{22}^{\star}$ converges to the thermal conductivity of Nb_3Sn at volume fraction 1 and the upper bound converges to the thermal conductivity of bronze at volume fraction 0. But transverse thermal conductivity $K_{22}^{\star}$ decreases nonlinearly as the increase of Nb_3Sn's volume fraction due to the inplane coupling effects.

After generating homogenized thermal conductivities of a filament group at microscale, the homogenized thermal conductivities of multiple filament groups can be obtained by analyzing a hexagonal RUC with a circular homogenized filament group embedded in the

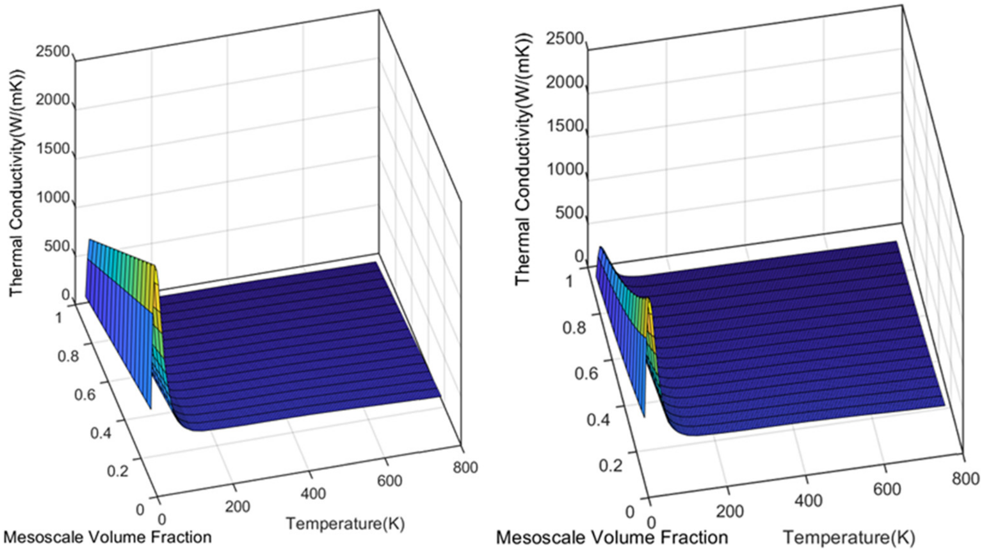

Figure 12: Effects of volume fraction of mesoscale homogenized Nb_3Sn filament group and temperature on the global homogenized thermal conductivity, (Left) $K_{11}^{\star}$, (Right) $K_{22}^{\star}(K_{33}^{\star})$. Note: Volume fraction 0.72 is specified for the microscale homogenized Nb_3Sn filament group.

bronze matrix. Figure 12 shows the effects of mesoscale volume fraction of the homogenized Nb_3Sn filament group on the global homogenized thermal conductivities between 5 and 800 K. The mesoscale homogenized thermal conductivity coefficients are first calculated with a given volume fraction of 0.72 between 5 and 800 K. Both the global homogenized axial and transverse thermal conductivities decrease as volume fraction of a homogenized filament group increases. The upper bound of thermal conductivity converges to the thermal conductivity of bronze and the lower bound of thermal conductivity converges to the thermal conductivity of mesoscale homogenized filament group at volume fraction 1. In contrast with the linear relation with the volume fraction for the axial thermal conductivity at a prescribed temperature, the homogenized transverse thermal conductivity varies nonlinearly with the volume fraction at a prescribed temperature.

5.2 Effects of volume fraction and temperature on homogenized mechanical properties and thermal expansion coefficients

Figures 13 and 14 illustrate the effect of volume fraction of a Nb_3Sn filament and temperature variation on the mesoscale homogenized mechanical properties, D_{11}^*, D_{22}^*, D_{33}^*, and thermal expansion coefficients, α_{11}^*, α_{22}^*, α_{33}^*, respectively. The maximum homogenized elasticity terms, D_{11}^*, D_{22}^*, D_{33}^*, occur at the lowest temperature level with only filament material Nb_3Sn and the minimum value occurs at the highest temperature level with only the bronze matrix. As filament volume fraction increases, the temperature influence on the homogenized mechanical properties decreases due to temperature insensitivity of Nb_3Sn. The maximum homogenized thermal expansion coefficients, α_{11}^*, α_{22}^*, α_{33}^*, occur at the highest temperature level with only the bronze matrix and the minimum value occurs at the lowest temperature with only filament phase, Nb_3Sn. Meanwhile, as the filament volume fraction increases, the temperature influence on the homogenized thermal expansion coefficients decreases because the filament phase Nb_3Sn is less sensitive to the temperature change.

Once the homogenized mechanical properties and thermal expansion coefficients of a filament group on the microscale are available, the global homogenized mechanical properties and thermal expansion coefficients of all the filament groups can be obtained by conducting thermomechanical homogenization towards the hexagonal RUC with a circular homogenized filament group embedded in the bronze matrix. Figures 15 and 16 illustrate the effect of mesoscale volume fraction and temperature variation on the global homogenized mechanical properties, D_{11}^*, D_{22}^*, D_{33}^*, and thermal expansion coefficients, α_{11}^*, α_{22}^*, α_{33}^*, respectively. During above calculation, the utilized volume fraction of a Nb_3Sn filament group at microscale is 0.42. The homogenized elasticity terms decrease as temperature increases due to the temperature

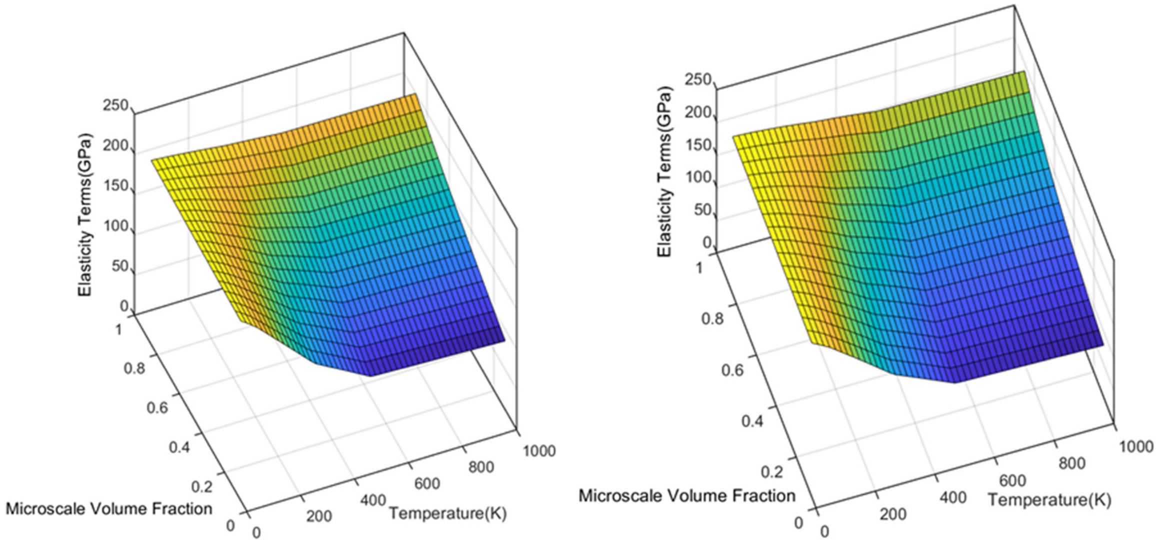

Figure 13: Effects of volume fraction of Nb_3Sn filament at microscale and temperature on mesoscale homogenized elasticity terms, (Left) D_{11}^*, (Right) $D_{22}^*(D_{33}^*)$.

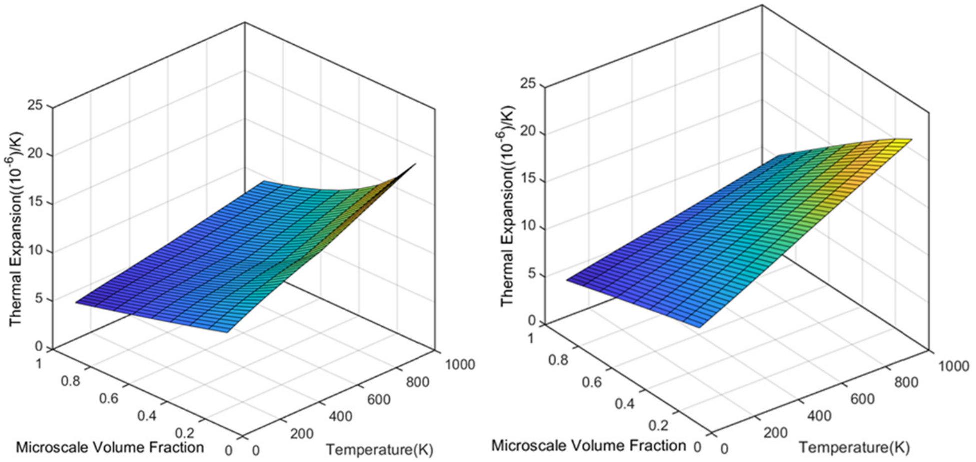

Figure 14: Effects of volume fraction of Nb_3Sn filament at microscale and temperature on mesoscale homogenized thermal expansion coefficients, (Left) α^*_{11}, (Right) $\alpha^*_{22}(\alpha^*_{33})$.

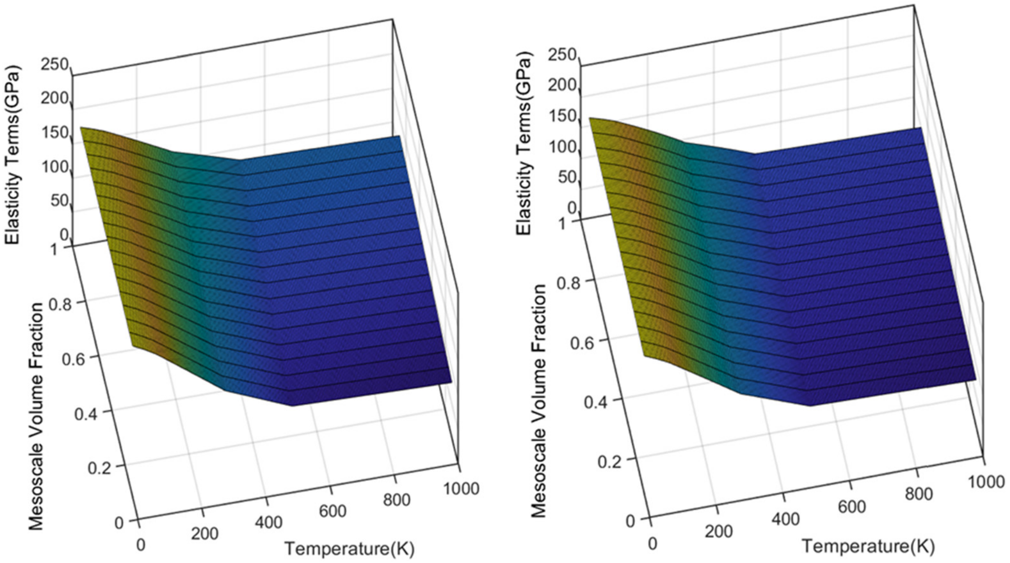

Figure 15: Effects of volume fraction of mesoscale homogenized Nb_3Sn filament group and temperature on the global homogenized elasticity terms, (Left) D^*_{11}, (Right) $D^*_{22}(D^*_{33})$. Note: Volume fraction 0.42 is specified for the microscale homogenized Nb_3Sn filament group.

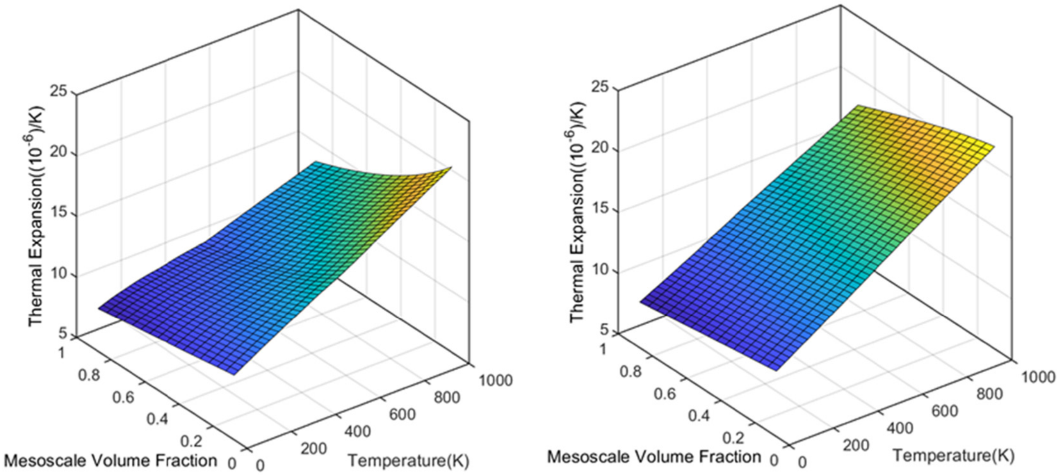

Figure 16: Effects of volume fraction of mesoscale homogenized Nb_3Sn filament group and temperature on the global homogenized thermal expansion coefficients, (Left) α^*_{11}, (Right) $\alpha^*_{22}(\alpha^*_{33})$. Note: Volume fraction 0.42 is specified for the microscale homogenized Nb_3Sn filament group.

softening effects on the bronze matrix and increase as the increase of volume fraction due to the increase of harder phase of Nb_3Sn. The global homogenized thermal expansion coefficients increase as the temperature increases due to the temperature effects on the bronze matrix and decrease as the increase of volume fraction due to the smaller mesoscale homogenized thermal expansion coefficients.

6 Conclusion

A comprehensive investigation of the homogenized thermal conductivity, mechanical properties, and thermal expansion coefficients has been conducted for the multiscale Nb_3Sn filament groups centered in an EAS strand utilized in ITER D-Shape magnet. The filament groups are modelled by two-scale repeating hexagonal unit cells *via* the Multiphysics LEHT, including thermal conductivity analysis and thermomechanical analysis. First, LEHT's results are validated against the Finite Element Analysis at both microscale and mesoscale homogenization. Then, a comprehensive parametric study is conducted for Nb_3Sn filament groups with the consideration of various volume fractions and temperature on both microscale and mesoscale thermal conductivities, mechanical properties, and thermal expansion coefficients. The principle conclusions of this investigation are as follows:

1. A comprehensive parametric study is conducted for the first time towards the effects of volume fraction and temperature variation on both mesoscale (a filament group) and global scale (multiple filament group) homogenized thermal conductivities, mechanical properties, and thermal expansion coefficients.
2. For the micro- and mesoscale thermal conductivity homogenization, the axial thermal conductivity decreases linearly as the increase of volume fraction of Nb_3Sn filament or its group, while the transverse thermal conductivity decreases nonlinearly.
3. For microscale homogenization of a group of Nb_3Sn filament, all elasticity terms increase, and all thermal expansion coefficients decrease as the increase of volume fraction, and both variations are much more sensitive to high temperature. For mesoscale homogenization of Nb_3Sn filament groups, all elasticity terms increase, and all thermal expansion coefficients decrease as the increase of volume fraction, but the variation is not sensitive to temperature change.
4. The power of the LEHT technique is not only proved by its accuracy in the multiscale analysis of Nb_3Sn filaments through a bottom-up procedure. As is also indicated in the text, the LEHT is also advantageous in its efficiency, which can be utilized and combined with reliable optimization techniques for the materials' design through a "top-down" procedure. Aiming at certain effective engineering requirements, the micromechanics-oriented optimization would provide a robust tool in varying the microstructural details, such as candidate materials and volume fractions. Most of those analytical scenarios can be even achieved through a PC instead of large-scale workstations.

Acknowledgment: Figures 1–3 in this paper are reprinted from: Boso DP *et al.* A multilevel homogenized model for superconducting strand thermomechanics. Cryogenics, 2005;45:257–271, [13], with permission from Elsevier.

Funding information: G. Wang acknowledges the support of National Natural Science Foundation of China (No. 12002303), the National Key Research and Development Program of China (No. 2020YFA0711701), and Fundamental Research Funds for the Central Universities (2020QNA4016). The corresponding author, W. Tu, acknowledges the support of Jiangsu University Research Initiation Fund for Senior Talents.

Author contributions: All authors have accepted responsibility for the entire content of this manuscript and approved its submission.

Conflict of interest: The authors state no conflict of interest.

References

[1] Sanabria C, Lee PJ, Starch W, Blum T, Devred A, Jewell MC, et al. Metallographic autopsies of full-scale ITER prototype cable-in-conduit conductors after full testing in SULTAN: 1. The mechanical role of copper strands in a CICC. Supercond Sci Technol. 2015;28(8):085005.

[2] Sanabria C, Lee PJ, Starch W, Devred A, Larbalestier DC. Metallographic autopsies of full-scale ITER prototype cable-in-conduit conductors after full cyclic testing in SULTAN: III. The importance of strand surface roughness in long twist pitch conductors. Supercond Sci Technol. 2016;29(7):074002.

[3] Gou X-F, Zhuo P-J, Zhou X-X, Schwartz J. Fractal-based analysis of the void microstructure of $Bi_2Sr_2CaCu_2O_x$ superconducting filaments and the caused anomalous thermal diffusion. Comput Mater Sci. 2019;158:219–27.

[4] Zhou X-X, Xue F, Gou X, Shen T-M. Statistical study of the void structure of Bi^- multifilamentary superconducting wires and

its effect on the critical current density. Eng Comput. 2019;36(8):2714–25.
[5] Lee GS, Kim J, Hwang SM, Chang CS, Chang HY, Cho MH, et al. The design of the KSTAR tokamak. Fusion Eng Des. 1999;46(2):405–11.
[6] Martovetsky N, Manahan R, Lieuke AF. Development of superconducting focusing quadrupoles for heavy ion drivers. IEEE Trans Appl Supercond. 2002;12(1):157–60.
[7] Schultz JH, Sujan GK. Superconducting wires and cables: high-field applications. Mater Sci Mater Eng. 2016.
[8] Sanabria C, Lee PJ, Starch W, Devred A, Larbalestier DC. Metallographic autopsies of full-scale ITER prototype cable-in-conduit conductors after full cyclic testing in SULTAN: II. Significant reduction of strand movement and strand damage in short twist pitch CICCs. Supercond Sci Technol. 2015;28(12):125003.
[9] ITER NEWSLINE. Europe completes D-shaped magnet; 2020 March 9. https://www.iter.org/newsline/-/3410
[10] Tsuji H, Okuno K, Thome R, Salpietro E, Egorov S, Martovetsky N, et al. Progress of the ITER central solenoid model coil programme. Nucl Fusion. 2001;41(5):645–51.
[11] Benjegerdes B, Bish P, Byford D, Caspi S, Chow K, Dietderich D, et al. Fabrication and test of Nb_3Sn racetrack coils at high field. IEEE Trans Appl Super. 2001;11(1):2164–7.
[12] Takeo M, Funaki K, Sato S, Yamafuji K, Iwakuma M, Hiramatsu M, et al. A 17 tesla superconducting magnet with multifilamentary superconductors. IEEE Trans Magn. 1987;23(2):565–78.
[13] Boso DP, Lefik M, Schrefler BA. A multilevel homogenised model for superconducting strand thermomechanics. Cryogenics. 2005;45(4):259–71.
[14] Liu B, Jing Z, Yong H, Zhou Y. Strain distributions in superconducting strands with twisted filaments. Compos Struct. 2017;174:158–65.
[15] Boso DP, Lefik M, Schrefler BA. Homogenisation methods for the thermo-mechanical analysis of Nb_3Sn strand. Cryogenics. 2006;46(7):569–80.
[16] Wang G, Pindera M-J. Locally-exact homogenization theory for transversely isotropic unidirectional composites. Mech Res Commun. 2016;78:2–14.
[17] Zhao J, Stenvall A, Gao Y, Salmi T. Analytical and numerical methods to estimate the effective mechanical properties of rutherford cables. IEEE Trans Appl Super. 2020;30(5):1–8.
[18] Mishnaevsky L Jr. Micromechanics of hierarchical materials: a brief overview. Rev Adv Mater Sci. 2012;30:60–72.
[19] Pindera M-J, Khatam H, Drago AS, Bansal Y. Micromechanics of spatially uniform heterogeneous media: a critical review and emerging approaches. Compos Part B Eng. 2009;40(5):349–78.
[20] Chen Q, Wang G, Pindera M-J. Homogenization and localization of nanoporous composites – a critical review and new developments. Compos Part B Eng. 2018;155:329–68.
[21] Charalambakis N. Homogenization techniques and micromechanics. a survey and perspectives. Appl Mech Rev. 2010;63(3):1–10.
[22] Wang G, Chen Q, Gao M, Yang B, Hui D. Generalized locally-exact homogenization theory for evaluation of electric conductivity and resistance of multiphase materials. Nanotechnol Rev. 2020;9(1):1–16.
[23] Weng GJ. A homogenization scheme for the plastic properties of nanocrystalline materials. Rev Adv Mater Sci. 2009;19(1–2):41–62.
[24] Feng J, Liang S, Guo X, Zhang Y, Song K. Electrical conductivity anisotropy of copper matrix composites reinforced with SiC whiskers. Nanotechnol Rev. 2019;8(1):285–92.
[25] Lee S-Y, Hwang J-G. Finite element nonlinear transient modelling of carbon nanotubes reinforced fiber/polymer composite spherical shells with a cutout. Nanotechnol Rev. 2019;8(1):444–51.
[26] Gao Z, Ren X, Zhang X. Prediction of effective properties for composite superconducting strand and multi-stage cables. Mater Today Commun. 2020;25:101674.
[27] Boso DP. A simple and effective approach for thermo-mechanical modelling of composite superconducting wires. Supercond Sci Technol. 2013;26(4):045006.
[28] Wang X, Gao Y. Tensile behavior analysis of the Nb_3Sn superconducting strand with damage of the filaments. IEEE Trans Appl Super. 2016;26(4):1–4.
[29] Lenoir G, Manil P, Nunio F, Aubin V. Mechanical behavior laws for multiscale numerical model of Nb_3Sn conductors. IEEE Trans Appl Super. 2019;29(5):1–6.
[30] Hu Q, Wang X, Guan M, Zhou Y. Magneto-mechanical coupling analysis of a superconducting solenoid using FEM with different approaches. IEEE Trans Appl Super. 2020;30(4):1–5.
[31] Drago AS, Pindera M-J. A locally exact homogenization theory for periodic microstructures with isotropic phases. J Appl Mech. 2008;75(5):0510101–4.
[32] Wang G. An efficient analytical homogenization technique for mechanical-hygrothermal responses of unidirectional composites with applications to optimization and multiscale analyses. Chin J Aeronaut. 2019;32(2):382–95.
[33] Wang G, Gao M, Yang B, Chen Q. The morphological effect of carbon fibers on the thermal conductive composites. Int J Heat Mass Transf. 2020;152:119477.
[34] Wang G, Pindera M-J. On Boundary condition implementation via variational principles in elasticity-based homogenization. J Appl Mech. 2016;83(10):101008.
[35] Chen Q, Pindera M-J. Homogenization and localization of elastic-plastic nanoporous materials with gurtin-murdoch interfaces: an assessment of computational approaches. Int J Plast. 2020;124:42–70.
[36] Chen Q, Wang G. Computationally-efficient homogenization and localization of unidirectional piezoelectric composites with partially cracked interface. Compos Struct. 2020;232:111452.
[37] Wang G, Chen Q, He Z, Pindera M-J. Homogenized moduli and local stress fields of unidirectional nano-composites. Compos Part B Eng. 2018;138:265–77.

Appendix

Herein, we list the governing/control equations that are solved through the present technique. The equilibrium equations in the cylindrical coordinate are expressed as [16,32,33]:

$$\begin{cases} \dfrac{\partial \sigma_{rr}}{\partial r} + \dfrac{1}{r} \cdot \dfrac{\partial \sigma_{r\theta}}{\partial \theta} + \dfrac{\partial \sigma_{rz}}{\partial z} + \dfrac{\sigma_{rr} - \sigma_{\theta\theta}}{r} = 0 \\ \dfrac{\partial \sigma_{r\theta}}{\partial r} + \dfrac{1}{r} \cdot \dfrac{\partial \sigma_{\theta\theta}}{\partial \theta} + \dfrac{\partial \sigma_{\theta z}}{\partial z} + \dfrac{2\sigma_{r\theta}}{r} = 0 \\ \dfrac{\partial \sigma_{rz}}{\partial r} + \dfrac{1}{r} \cdot \dfrac{\partial \sigma_{\theta z}}{\partial \theta} + \dfrac{\partial \sigma_{zz}}{\partial z} + \dfrac{\sigma_{rz}}{r} = 0 \end{cases} \tag{A1}$$

where $\sigma_{kl}\,(k, l = r, \theta, z)$ is the stress components. Substitution of stress–strain and strain-displacement relations into equation (A1) further leads to the Navier's equations under general plane strain assumption:

$$\begin{cases} \dfrac{\partial^2 u_z'}{\partial r^2} + \dfrac{1}{r} \cdot \dfrac{\partial u_z'}{\partial r} + \dfrac{1}{r^2} \cdot \dfrac{\partial^2 u_z'}{\partial \theta^2} = 0 \\ C_{22}\left(\dfrac{\partial^2 u_r'}{\partial r^2} + \dfrac{1}{r} \cdot \dfrac{\partial u_r'}{\partial r} - \dfrac{u_r}{r^2}\right) + \dfrac{C_{22} - C_{23}}{2r^2} \cdot \dfrac{\partial^2 u_r'}{\partial \theta^2} + \dfrac{C_{22} + C_{23}}{2r} \cdot \dfrac{\partial^2 u'_\theta}{\partial r \partial \theta} - \dfrac{3C_{22} - C_{23}}{2r^2} \cdot \dfrac{\partial u'_\theta}{\partial \theta} = 0 \\ \dfrac{C_{22} - C_{23}}{2}\left(\dfrac{\partial^2 u'_\theta}{\partial r^2} + \dfrac{1}{r} \cdot \dfrac{\partial u'_\theta}{\partial r} - \dfrac{u_\theta}{r^2}\right) + \dfrac{C_{22}}{r^2} \cdot \dfrac{\partial^2 u'_\theta}{\partial \theta^2} + \dfrac{C_{22} + C_{23}}{2r} \cdot \dfrac{\partial^2 u'_r}{\partial r \partial \theta} + \dfrac{3C_{22} - C_{23}}{2r^2} \cdot \dfrac{\partial u'_r}{\partial \theta} = 0 \end{cases} \tag{A2}$$

where the prime superscript stands for the fluctuating components of equations (4a–4c). C_{22} and C_{23} are the stiffness matrix components. In a similar manner, the control equation for conduction is expressed as [33]

$$\frac{\partial}{\partial z}\left(k_{zz}\frac{\partial T'}{\partial z}\right) + \frac{1}{r}\frac{\partial}{\partial r}\left(k_{rr} r \frac{\partial T'}{\partial r}\right) + \frac{1}{r^2}\frac{\partial}{\partial \theta}\left(k_{\theta\theta}\frac{\partial T'}{\partial \theta}\right) = 0 \tag{A3}$$

where $k_{ii}(i = r, \theta, z)$ are the conductivity coefficients in the cylindrical coordinate and can be transformed to Cartesian coordinate through coordinate transformation relations.